

Charge Transfer Simulations using Hamiltonian Elements and Forces from Neural Networks

Philipp M. Dohmen,^{†,‡,⊥} Mila Krämer,^{†,⊥} Patrick Reiser,[¶] Pascal Friederich,^{¶,§}
Marcus Elstner,^{†,‡} and Weiwei Xie^{*,||}

[†]*Institute of Physical Chemistry (IPC), Karlsruhe Institute of Technology, 76131
Karlsruhe, Germany*

[‡]*Institute of Biological Interfaces (IBG2), Karlsruhe Institute of Technology, 76131
Karlsruhe, Germany*

[¶]*Institute of Nanotechnology (INT), Karlsruhe Institute of Technology, 76131 Karlsruhe,
Germany*

[§]*Institute of Theoretical Informatics (ITI), Karlsruhe Institute of Technology, 76131
Karlsruhe, Germany*

^{||}*Key Laboratory of Advanced Energy Materials Chemistry (Ministry of Education),
Renewable Energy Conversion and Storage Center, College of Chemistry, Nankai
University, Tianjin, 300071, China*

[⊥]*These authors contributed equally to this work.*

E-mail: xieweiwei@nankai.edu.cn

Abstract

1 Introduction

Molecular organic semiconductors (OSCs) have become ubiquitous components of electronic devices, in the forms of organic light emitting diodes (LEDs) in modern display technologies¹⁻³, organic field effect transistors⁴⁻⁶, or organic photovoltaic devices⁷⁻⁹. Compared to the silicon-based technologies for LEDs, transistors, or photovoltaic devices, OSCs are inexpensive and easier to manufacture and process¹⁰. With the near-limitless variety of organochemical compounds, searching for novel candidates with specific properties or optimizing known materials is a costly process. Here, theoretical approaches using simulation techniques can supplement or shorten experimental studies by efficiently screening large portions of chemical space for compounds with promising properties before committing to synthesizing them. This requires fast and robust methods for simulating charge and exciton transfer in large molecular systems which can reproduce experimentally observable quantities such as charge carrier mobilities.

Simple models used to describe the transfer of charges and excitons assume either a band-like or hopping-like regime¹¹. In the band model, the charge is strongly delocalized as the couplings between the charge carriers are large and the reorganization energy is small. In contrast, hopping-like transfer occurs when the reorganization energy is large and the coupling is small, creating an activation barrier which is only overcome via thermal fluctuations. This results in a strong localization of the charge on single molecules, and transfer occurs in discrete hops.

In OSCs, however, neither of these approximations hold¹¹, and direct simulations using quantum-chemical (QM) methods are needed to describe the transfer process properly. These approaches use non-adiabatic molecular dynamics (NAMD) methods and explicitly take into account the electronic degrees of freedom by solving the time-dependent Schrödinger equation (TDSE)¹²⁻¹⁵. To mitigate the computational costs inherent in a quantum-chemical description of large systems along extensive molecular dynamics (MD) trajectories, the nuclei are treated classically and the electronic structure of the individual molecules is simplified.

Using a conceptual coarse-graining of the transfer process, the electronic structure of the entire system can be compacted to two core parameters: the energies of frontier orbitals on each molecule and the pairwise coupling terms which describe their interaction. The response of a molecule to a change in its occupation can be taken into account explicitly by approximating the forces in the charged state. Alternatively, this relaxation can be modeled *implicitly* by artificially reducing its energy by an empirically determined reorganization energy.

Still, the costs of the *ab initio* or semi-empirical models used to describe the electronic structure can be prohibitively large when the system size and trajectory lengths needed to accurately obtain observables are taken into account. Data-driven approaches, more specifically machine learning (ML) methods, can make use of the fact that the quantum-chemical calculations are highly repetitive, i.e. the conformations sampled during such simulations are very similar. By training the ML model on a small but representative data set for which the relevant electronic parameters have been calculated using a quantum chemistry method, the computationally simpler ML method could then be used to drive the transfer simulations. Several works have previously investigated the applicability of ML models to charge and exciton transfer properties: Both kernel ridge regression (KRR)¹⁶⁻¹⁸ and neural network (NN) models^{19,20} have been used for predicting charge transfer couplings in organic and metal-organic systems. For excitonic properties, neural networks have been used to predict excitation energies in biological systems²¹, and there has been extensive work on ML-driven excited-state molecular dynamics²²⁻²⁵ for small organic molecules.

In our previous work¹⁸, we used KRR models for predicting site energies and couplings in anthracene for both charge and exciton transfer applications. By using the fast and accurate density-functional tight binding (DFTB) method²⁶⁻³² to generate reference data cheaply and automating model training we created a scheme which was easily applicable to new systems without requiring individual models to generalize across chemical space. We then applied these models in propagation simulations, comparing the resulting observables with

experimental or higher-level computational data. Our models were able to reproduce hole mobilities close to the reference and experimental values when using the mean-field Ehrenfest (MFE) propagator using the implicit relaxation scheme with a fixed reorganization energy. When using the Boltzmann-corrected fewest-switches surface hopping (BC-FSSH) method for propagation, we observed that while the ML method was close to the appropriate DFTB reference, both were far off from the values obtained if molecular relaxation was explicitly taken into account.

While the implicit relaxation scheme has since been improved [citation needed] to give better mobilities, it is still an approximation which only has limited applicability in systems where the assumption that the molecules relax instantly does not hold.

can we specify this further?

Therefore, obtaining the occupation-dependent forces required for molecular relaxation from a machine-learning model is an obvious next step. These forces can be considered as a correction to the neutral-state forces provided by the force-field (FF) driving the nuclear dynamics in the simulation and obtained as derivatives of the site energies from the Hamiltonian used for propagation with respect to the atomic positions. Unfortunately, obtaining a prediction of a property and its derivatives w.r.t. the inputs from a KRR model is tricky. Efforts to extend the KRR formalism to this end³³ were unsuitable for our application due to the high computational costs they incur.

In this work, we therefore present neural network based models which are able to predict not just site energies and couplings but also the gradients of the site energy necessary for occupation-dependent forces. We restrict ourselves to simulations of charge transfer and train the models on DFTB-quality data for both anthracene and pentacene. By using the obtained models in propagation simulations, we can evaluate their performance in reproducing hole mobilities in these materials in terms of both quality and computational cost.

2 Methods

2.1 Background

2.1.1 Charge Transfer Simulations

In order to make charge transfer simulations feasible, the degrees of freedom (DOF) which receive full quantum-mechanical treatment must be reduced as much as possible. In our simulations we therefore treat the nuclear degrees of freedom classically using Newton’s equations of motion and a molecular mechanics (MM) force field. The electronic degrees of freedom are calculated quantum-mechanically and the time-dependent Schrödinger equation is used to calculate electronic dynamics³⁴. To further reduce computational costs, we make use of the weakness of the non-covalent interactions between individual molecules, as the orbital structure of two molecules in proximity to each other can be assumed to be essentially identical to that of the isolated molecules. This approximation allows us to split the system into molecular fragments and obtain the electronic structure of each fragment in a separate QM calculation. The wave function for transport of the hole or electron is then expressed as a linear combination of orthogonal molecular orbitals (MOs) $|\phi_m\rangle$ localized on individual fragment molecules A :

$$\Psi = \sum_A \sum_{m \in A} a_m |\phi_m\rangle \quad (1)$$

This is called the fragment molecular orbital (FMO) approach. Only the frontier MOs (m) of the fragments are considered¹³, as charge transfer in OSCs occurs in a narrow energy band around the Fermi level. The energies of these frontier MOs for each fragment and the pairwise couplings between them can be used to construct a coarse-grained Hamiltonian for propagation of the electronic DOF^{35,36} as

$$H_{mn}^0 = \langle \phi_m | \hat{H}[\rho_0] | \phi_n \rangle , \quad (2)$$

where $\hat{H}[\rho_0]$ is obtained from the QM calculations of the fragments. The *diagonal* elements of the coarse-grained Hamiltonian are on-site-terms (site energies), while its *off-diagonal* elements are pairwise couplings between the fragments. They can be obtained with only a slight increase in computational cost, involving only the relevant frontier orbitals. The Hamiltonian can then be used in one of the commonly used propagation algorithms, such as the mean-field Ehrenfest method^{37,38} (MFE) or variations of the fewest-switches surface hopping^{39,40} (FSSH) method to solve the coupled equations of motion for electronic and nuclear DOF.

In this work, we used a variant of FSSH using a Boltzmann correction instead of non-adiabatic coupling vectors for velocity re-scaling. In the FSSH method, the electronic wave function is expressed as a linear combination of adiabatic basis functions $\{|\psi_i\rangle\}$:

$$\Psi = \sum C_i^{\text{ad}} |\psi_i\rangle, \quad (3)$$

where C_i^{ad} are the expansion coefficients of the electronic wave function in the adiabatic representation. Inserting Eq. 3 into the time-dependent Schrödinger equation and projecting onto the adiabatic electronic basis states, we obtain

$$i\hbar \frac{dC_j^{\text{ad}}}{dt} = C_j^{\text{ad}} H_j^{\text{ad}} - i\hbar \sum_k C_k^{\text{ad}} \dot{\mathbf{R}} \mathbf{d}_{jk}, \quad (4)$$

where \mathbf{d}_{jk} denotes the non-adiabatic coupling vector (NCV) and H_j^{ad} is the potential energy (PE) of adiabatic state j . The diagonalization of the matrix \mathbf{H}^0 yields the adiabatic potential energies

$$\mathbf{H}^{\text{ad}} = \mathbf{U}^\dagger \mathbf{H}^0 \mathbf{U}, \quad (5)$$

where \mathbf{U} is the diabatic-to-adiabatic transformation matrix.

Classical trajectories are propagated on a single electronic state according to Newton's

cite
also
blum-
berger
for
jfssh?

equations of motion:

$$\begin{aligned}
 m_k \ddot{R}_k &= -\frac{\partial E_{\text{MM}}^{\text{tot}}}{\partial R_k} + \frac{\partial H_j^{\text{ad}}}{\partial R_k} - \frac{\partial \Delta E^{\text{QM/MM}}}{\partial R_k} \\
 &= -\frac{\partial E_{\text{MM}}^{\text{tot}}}{\partial R_k} + \sum_{mn} U_{am} U_{an} \frac{\partial H_{mn}^0}{\partial R_k} - \frac{\partial \Delta E^{\text{QM/MM}}}{\partial R_k},
 \end{aligned} \tag{6}$$

where H_j^{ad} denotes the adiabatic energy of the current state j .

The hopping probability from the current state j to another state k is defined as

$$P_{\text{FSSH}}^{j \rightarrow k} = \max \left\{ 0, \frac{2 \dot{\mathbf{R}} \cdot \mathbf{d}_{jk} \text{Re}(C_k^{\text{ad}*} C_j^{\text{ad}})}{|C_j^{\text{ad}}|^2} \Delta t \right\}. \tag{7}$$

A uniform random number ξ between 0 and 1 is generated and a switch from state j to state k takes place, if

$$\sum_{i=1}^{k-1} P_{\text{FSSH}}^{j \rightarrow i} < \xi \leq \sum_{i=1}^k P_{\text{FSSH}}^{j \rightarrow i}. \tag{8}$$

To ensure the conservation of total energy for each trajectory, the nuclear momenta must be adjusted when a hop occurs. This is usually achieved by re-scaling the nuclear velocities to compensate the change of the PE. While distributing this effect isotropically across all velocity components is possible, better results are obtained if the velocities are re-scaled in the direction of the non-adiabatic coupling vectors.⁴⁰ If the adjustment of momentum is not sufficient to compensate the change in PE (an ‘energy-forbidden’ or ‘frustrated’ hop), the trajectory continues in the original electronic state j , and the momenta along the NCV are reversed.

An alternative to using NCVs is to re-scale the hopping probability using the Boltzmann factor $\exp\left(-\frac{H_k^{\text{ad}} - H_j^{\text{ad}}}{k_B T}\right)$ ⁴¹ and leave the velocities unchanged. This Boltzmann-corrected FSSH method has the advantage that computationally demanding NCVs are not necessary, while giving better results than isotropic re-scaling [\[citation needed\]](#).

After a hop occurs, fragments occupied by the charge carrier must respond to the changed electronic state by relaxing their geometry, which reduces their site energies. As mentioned

what
is a?
ex-
plain
the
other
vari-
ables?

above, this can either be accomplished by artificially lowering the site energy by an empirically determined value for the reorganization energy, or by applying the forces resulting from the charged state. As the force field which governs nuclear dynamics is parameterized to reproduce the forces in the neutral state, the forces for occupied fragments can be adjusted using the difference between forces in the neutral and charged states. Note that this approach is different from the adiabatic forces used in other non-adiabatic dynamics methods.

Under the approximation that the electronic structure of the charged fragments is identical to that of the neutral molecules except for the occupations of the individual orbitals we can obtain the difference between charged and neutral state forces as the forces resulting from only the frontier orbitals in which the occupations change. These *FMO*-forces are the exact derivatives of the diagonal and off-diagonal terms in the CT Hamiltonian. As the coupling with neighboring fragments only results in small force contributions compared to the FF and diagonal terms, we neglect the off-diagonal derivatives in this work. In the future, the off-diagonal derivatives can be used for both relaxation and calculating non-adiabatic coupling vectors.

Another way to obtain the force correction necessary for relaxation is to calculate the forces from the charged molecule’s electronic state in addition to the neutral-state calculation and form the difference between the forces in the two states.

$$F^\Delta = \frac{\partial}{\partial R_k} E^{\text{charged}} - \frac{\partial}{\partial R_k} E^{\text{neutral}}. \quad (9)$$

This Δ -force approach however requires an additional QM calculation of the charged fragment, which is why it is not usually used during propagation simulations.

In all systems examined in this work, the occupation-dependent QM forces were approximately one order of magnitude smaller than the FF baseline. This is quite helpful when replacing the QM method with an ML model, as it provides a larger margin of error for predictions before they significantly impact the stability of the simulation by creating physically

difficult
to
support
when
we
don't
trust
DFTB
offdiag
forces

unreasonable geometries.

2.1.2 Machine Learning Methods

Neural networks are non-linear statistical models which are widely used to solve complex regression or classification problems. A feed-forward neural networks takes a vector of inputs $(x_1, x_2, \dots x_i)$ and makes a number of linear combinations $(n_1, n_2, \dots n_j)$ of these inputs referred to as neurons. The weights w_{ij} determine the contribution of each input i to each combination j . The result of each linear combination n is then passed through a non-linear activation function, which allows the neural network to approximate arbitrarily complex functions. These results are then combined to make another layer of linear combinations, and the process can be repeated until the desired network depth is reached. The final layer of the network then carries the results, i.e. the prediction the network makes for a given input.

All weights in the NN are initialized randomly and adjusted such that the prediction for inputs for which the result value is known matches the reference value as closely as possible as measured by a metric referred to as *cost* function. Cost functions can be as simple as the mean squared error (MSE) between prediction or reference, but can also include other terms to impose additional constraints on the structure of the network. Training is then the process of minimizing the cost function by giving the network inputs from the training data set and evaluating the cost. Minimization uses the backpropagation algorithm, in essence taking the derivative of the cost function w.r.t. all weights in the network (employing the chain rule for deep networks with multiple layers) repeatedly and making small steps towards the minimum of the function.

The choices made in the construction of the network (e.g. how many layers and neurons to use) can strongly influence the performance of the resulting models. As these parameters are not optimized during the training itself, the proper values for them must be determined by another process, and they are referred to as *hyperparameters*. Hyperparameter optimiza-

tion usually requires repeated training of NNs on the same data set while the values for the hyperparameters are varied. This is usually computationally demanding, as the search space can grow rather large very quickly, and can be performed using various optimization algorithms.

2.2 Computational Details

2.2.1 Generation of training data

The procedures for generating training data were identical for both the anthracene and pentacene systems. For each system, we created a crystal super-cell based on experimental crystal structures⁴² [citation needed]. The anthracene super-cell contained $8 \times 8 \times 5$ molecules along the crystal axes (a , b and c), respectively. In pentacene, the size of the crystal was $8 \times 16 \times 5$ molecules.

Force field parameters for each system were derived from the general AMBER force field (GAFF)^{43,44}. Atomic charges were generated from the restrained electrostatic potential (RESP) fitting procedure^{45,46}, calculated at HF/6-31G*^{47,48} level of theory using Gaussian09⁴⁹.

After an initial energy minimization the temperature was equilibrated for 1 ns with a time step of 2 fs using the Nose-Hoover thermostat⁵⁰ at 500 K. Subsequently, productive MD simulations were run for 1 ns with a time step of 1 fs, in which structures were saved every 1 ps. All MD simulations were performed with the GROMACS 4.6 software package^{51,52}.

As the gradients obtained from the ML methods will be used to relax molecular geometries, it is crucial that gradient predictions are reliable across the entirety of the potential energy surfaces (PES) accessible throughout the simulation. In order to keep the learning procedure and implementation of ML predictions into the simulation code simple, we refrained from using active learning or similar techniques. Instead, we constructed the training data set by sampling geometries along both the PES of the neutral system and the charged system at a temperature higher than that used during the productive simulations

cite
for
pen-
tacene
struc-
ture

for obtaining mobilities. One standard MD simulation was done to sample geometries on the neutral PES, while multiple separate NAMD simulations were performed to sample on the PES of positively charged molecules. Here, the charge was constrained to one molecule. The final data set then contained data from both neutral and charged PES in a 50:50 ratio.

Eventually, single molecule structures and pair-structures sampled in the neutral and charged states were randomly selected from a $5 \times 5 \times 3$ molecular cube in the center of the crystal for subsequent calculations of site energies, their derivatives and couplings. The HOMO was chosen as the frontier orbital for hole transport. Site energies and electronic couplings were calculated using non-self-consistent DFTB^{26,27}, often referred to as DFTB1. For the derivatives of the site energy, different data sets were constructed corresponding to the two approaches to obtain the gradients discussed in subsection 2.1.1. The *FMO* gradients are obtained as gradients of the HOMO of the neutral molecule using DFTB1. In contrast, the Δ gradients were obtained as the difference between the total gradients of the neutral and charged molecules using self-consistent-charge DFTB²⁸ with a long-range corrected functional⁵³ (LC-DFTB2) as implemented in the `dftb+` (version 19.1)^{31,32} program. We used LC-DFTB2 for this data set, as the long-range corrected functional can correct the underestimation of the reorganization energies observed when using the GGA-derived non-self-consistent DFTB. [citation needed] Additionally, gradients for anthracene are obtained from DFT calculations with the B3LYP⁵⁴ and ω B97X⁵⁵ functionals, employing the def2-TZVP⁵⁶ basis-set together with the def2/J⁵⁷ auxiliary basis as implemented in `orca` (version 5.0.1)^{58,59}.

2.2.2 Training of Machine Learning Models

We adapt the neural network architecture previously presented by Li et al.²² for our application, as it has been constructed in order to predict energies and forces electronic states of small organic molecules. The network uses as inputs the spatial coordinates of the atoms in the system, from which inverse interatomic distances between atoms are calculated as

a translationally and rotationally invariant representation. In models predicting the site energies and their derivatives, all intramolecular interatomic distances are included in the representation. For the coupling models, we use only the intermolecular block of the matrix of inverse distances as this has been shown to be superior for predicting coupling elements¹⁷ and reduces the computational cost of each prediction¹. The trainable part of the network is a multi-layer dense feed-forward NN using the leaky softplus activation function ($f(x) = (1 - \alpha) \cdot \text{softplus}(x) + \alpha \cdot x$)⁶⁰ with a slope $\alpha = 0.03$.

Models were trained using the `pyNNsMD` package²² and Tensorflow 2.3⁶¹ with the Keras API⁶². Weights were optimized using the Adam optimizer⁶³ and mean-squared-error loss. All models received training and validation data in a 9:1 ratio, and the loss on the validation set was monitored every epoch, so training could be stopped when it did not improve for more than 100 epochs (early stopping). Feature calculation and scaling are both implemented as layers of the neural network, reducing implementation overhead when using the models for prediction. While training the models for the couplings was straightforward, during training of the site energy models the loss was calculated on both the network’s prediction and the gradients w.r.t. input coordinates. The relative weights of these two parts of the loss function were considered a hyperparameter of the model.

We used the Hyperband algorithm as an efficient and automatable way to find working combinations of hyperparameters⁶⁴. However, the quality of the resulting models was only weakly dependent on the chosen hyperparameters, indicating that a thorough hyperparameter search is unnecessary and can be omitted when applying the method to new systems. More details on the network configuration, training and hyperparameter search can be found in the supporting information.

¹Our initial experiments confirmed that the reduced representation gives lower errors at all training set sizes

2.2.3 Charge Transfer Simulations

We generated separate crystals for the transfer simulations containing $40 \times 30 \times 14$ (36) molecules for anthracene in a -direction, $20 \times 40 \times 5$ (36) molecules for anthracene in b -direction and $42 \times 84 \times 3$ (73) molecules for pentacene in $T1$ -direction. We chose one-dimensional lines of molecules along the respective directions in the middle of each crystal for the QM zone, with the number of fragments specified in brackets. After equilibration at 300 K structures in equidistant time intervals of 10 ps were chosen as starting structures for subsequent simulations of charge transfer. The hole wave function was initially localized on the first molecule. We used a time step of 0.100 fs for the propagation of nuclei, the TDSE was integrated numerically with the fourth-order Runge-Kutta algorithm with an integration time step of 0.010 fs. Averages of observables were calculated on 1000 trajectories, which were simulated for 1 ps each, while the first 0.350 fs were regarded as initial equilibration of the charge. All charge transfer simulations were performed within a local version of GROMACS 4.6 where DFTB, NN as well as the BC-FSSH methods were implemented.

We calculated the hole mobility μ with the Einstein-Smoluchowski equation⁶⁵ as

$$\mu = \frac{eD}{k_B T}, \quad (10)$$

where e is the elementary charge, k_B is the Boltzmann constant and T denotes the temperature. The diffusion coefficient D ⁶⁶ is

$$D = \frac{1}{2n} \lim_{t \rightarrow \infty} \frac{d\text{MSD}(t)}{dt}, \quad (11)$$

where n is the dimensionality ($n = 1$ for a one-dimensional chain). The mean square displacement (MSD) of the charge across N_{traj} trajectories is then

$$\text{MSD}(t) = \frac{1}{N_{\text{traj}}} \sum_l^{N_{\text{traj}}} \sum_A (x_A(t)^{(l)} - x_0^{(l)})^2 P_A^{(l)}(t), \quad (12)$$

where $x_A(t)^{(l)}$ and $P_A(t)^{(l)}$ are the center of mass of molecule A and the corresponding diabatic population along the trajectory l , respectively. $x_0^{(l)}$ is the center of charge at $t = 0$.

3 Results

3.1 Model Training and Evaluation

After training the models as described in subsection 2.2.2, we evaluated how well they were able to predict held-out test data from their respective reference data set. All trained models converged well within two thousand epochs, with prediction errors shrinking as training set sizes increased. In contrast to the KRR models used in our previous work, the NN models were able to learn the sign of the couplings even at low training set sizes. Overall, the hyperparameters included in the search had only a negligible influence on the quality of models obtained compared to the statistical noise from the initialization of the weights. While it is possible that specific hyperparameter configurations might also reduce the number of epochs needed until convergence, the added computational cost of the hyperparameter search far exceeds these gains. We therefore conclude that for this application, a full hyperparameter search can be omitted.

Here, we summarize the evaluation results for the models which we used in the propagation simulations in subsection 3.2. These models were obtained using a training set size of 30 000 structures each, with 3333 additional structures used for validation and the optimal hyperparameter configurations resulting from the hyperparameter search. Metrics were evaluated on 10 000 structures not used during training. The full results of the hyperparameter search and evaluation of individual models can be found in the supporting information.

3.1.1 Anthracene

Table 1 gives a few crucial metrics for the models trained on the anthracene data. All models give excellent predictions with few outliers, as can be seen in Figure 1. The model for the

metrics
for
B3LYP
and
 ω B97X

Table 1: Quality metrics for anthracene models.

	FMO			Δ -LC	
	coupling	site energy	gradient	site energy	gradient
MAE [meV(\AA)]	1.772	2.554	10.581	9.467	41.130
max err [meV(\AA)]	48.349	18.207	257.772	50.091	533.835
R^2	0.955	0.998	0.998	0.975	0.986

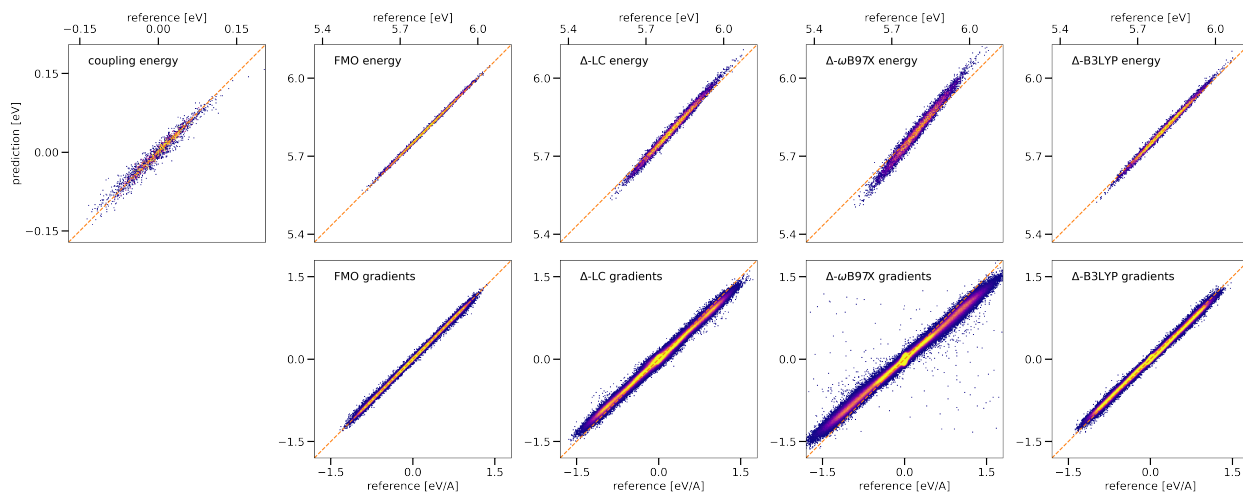


Figure 1: Two-dimensional histogram of model predictions vs. DFTB target for 10 000 structures in Anthracene. Bright colors indicate high data density, unoccupied areas shown white.

couplings in anthracene performed quite well, reaching low mean absolute errors (1.772 meV) with an R^2 score of 0.955. For the FMO site energies and their gradients, the model reached a MAE of 2.554 meV for the energies and 10.581 meV/Å for the gradients, with R^2 scores above 0.998 for both. The model trained on the Δ -LC data gave slightly worse results, and in contrast to the model for the FMO data did not perform equally well for both energies and gradients. This is a direct result from the construction of the LC data set, where LC-DFTB is only used to calculate the gradients, and these are learned in conjunction with the FMO site energies.

The errors for site energies and couplings are comparable to those obtained for similar training set sizes in our previous work, indicating that the models should be sufficiently accurate to give good mobilities in simulations. The effects of the error on the forces cannot be so easily quantified, but the maximum prediction errors can be an indication whether the predicted forces could impede the stability of the simulation. The maximum prediction errors for both the FMO (0.258 eV/Å) and Δ -LC gradients (0.534 eV/Å) are well below the forces needed to break covalent bonds (≈ 1 eV/Å to 2 eV/Å⁶⁷). Overall, these large errors are only seen for a few individual outliers, as less than one percent of gradient predictions show errors above 40 meV/Å (FMO) or 160 meV/Å (Δ -LC). These metrics indicate that the gradient predictions should be sufficiently reliable for performing molecular dynamics.

3.1.2 Pentacene

In pentacene, the results were quite similar and are summarized in Table 2 and visualized in Figure 2. In Pentacene, the couplings along the different crystal directions are quite dissimilar, leading to the bimodal distribution seen in the upper left of Figure 2 and a more difficult learning target for the ML model. As the mean magnitude of couplings is in the pentacene data set is 28.208 meV compared to 7.845 meV in anthracene, the MAE of the coupling predictions in pentacene is greater. The highly similar R^2 scores between the two systems indicate that the models have captured the data set equally well. The prediction

Table 2: Quality metrics for pentacene models.

	FMO			Δ -LC	
	coupling	site energy	gradient	site energy	gradient
MAE [meV(/ \AA)]	5.520	3.434	17.086	5.549	41.003
max err [meV(/ \AA)]	68.075	22.456	239.181	31.647	414.127
R^2	0.958	0.990	0.988	0.974	0.959

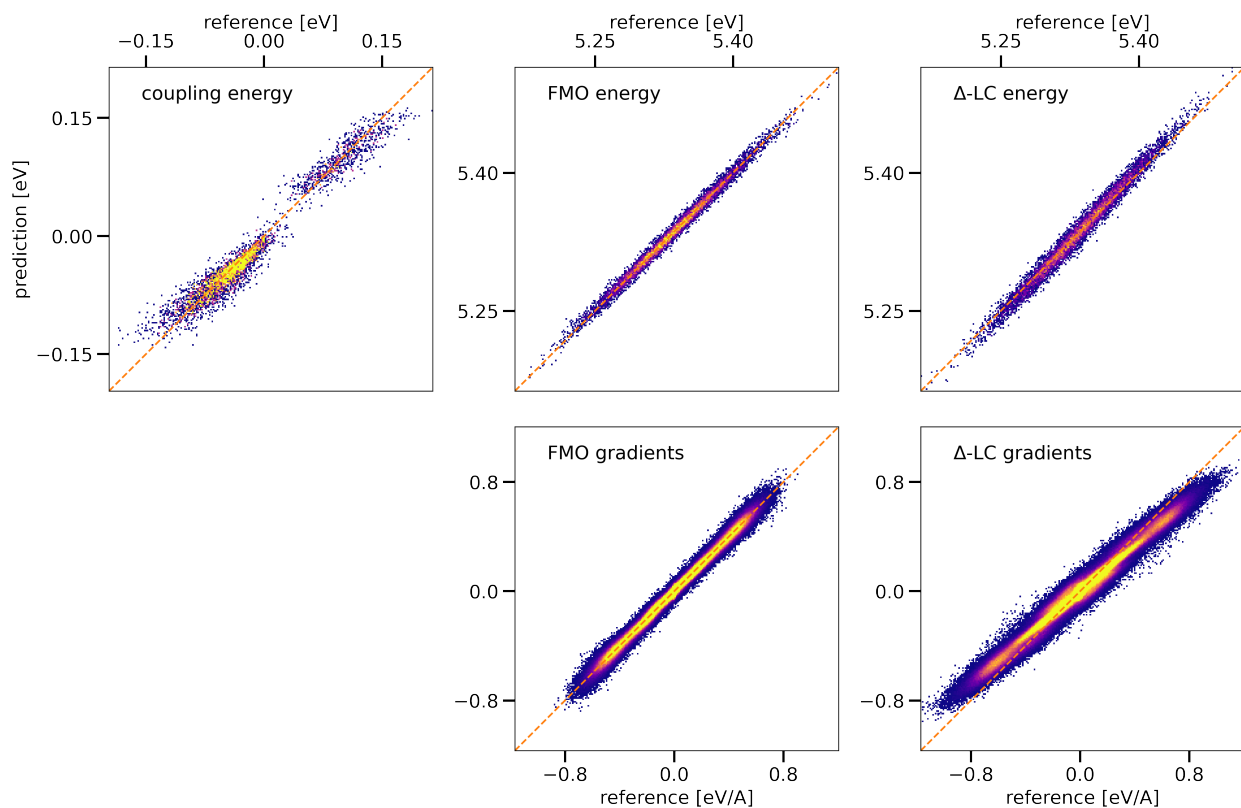


Figure 2: Two-dimensional histogram of model predictions vs. DFTB target for 10 000 structures in Pentacene. Bright colors indicate high data density, unoccupied areas shown white.

errors for site energies and their gradients in the pentacene system were slightly worse than for the anthracene models, but still excellent. Maximum prediction errors for the gradients were slightly lower than in anthracene, and the error distribution remained narrow.

3.2 Machine-Learning Driven Simulations

3.2.1 Accuracy of Obtained Observables

In the following, we use the trained neural network models to perform NAMD simulations of hole transfer along linear chains of anthracene molecules in *a*- and *b*-direction as well as pentacene molecules in *T1*-direction. These simulations are analyzed in terms of accuracy in reproducing hole mobilities compared to the reference method (DFTB) and experimentally determined values.

In order to perform stable NAMD simulations, where the nuclear dynamics are partly driven by machine learned models, it turned out to be necessary to sample geometries for training data on the PES of both neutral and charged molecules. First tests with models trained on geometries in the neutral state only led to unstable/crashing simulations. Adding geometries that were sampled in the charged state gave robust models and stable simulations, such that no catastrophically bad predictions occurred in the more than 100 million simulation time steps performed for this work. As the occupation-dependent force corrections are approximately one order of magnitude smaller than the forces from the MM force field, the margin of error that the ML models can make before simulation stability is impacted is quite large and no further efforts (e.g. active learning) were necessary.

The NAMD simulations presented here are driven by models, which are trained on the same diagonal energies but different gradients for relaxation, calculated either with FMO-DFTB1 (FMO), Δ -LC-DFTB2 (Δ -LC), Δ -DFT/B3LYP (Δ -B3LYP) or Δ -DFT/ ω B97X (Δ - ω B97X). All ML driven simulations use the same molecule specific models for the prediction of off-diagonal energies. Additionally, DFTB driven simulations are performed as our reference method, using FMO-gradients for the relaxation. All other approaches are not

implemented and computationally too demanding. The calculated hole mobilities for all investigated systems are displayed in Table 3, which are computed from the corresponding averaged time-dependent MSD (given in Figure ?? in the Supporting Information).

Table 3: Calculated and experimental hole mobilities (in $\frac{cm^2}{Vs}$) for anthracene (a - and b -direction) and pentacene ($T1$ -direction). Simulations are driven by Hamiltonians and diagonal gradients from DFTB or NN models, the latter are trained on different diagonal gradients from DFTB (FMO, Δ -LC) and DFT (Δ -B3LYP, Δ - ω B97X), respectively.

Method	Relaxation	ANT-a	ANT-b	PEN-T1
DFTB	FMO	3.2	8.4	11.6
NN	FMO	2.9	8.7	14.6
	Δ -LC	2.7	8.1	14.2
	Δ -B3LYP	2.5	8.1	-
	Δ - ω B97X	1.9	5.8	-
Experiment		1.1 ⁶⁸	2.9 ⁶⁸	10.5 ⁶⁹

Comparing mobilities from NN model driven simulations with the those from DFTB reference simulations (both using FMO forces), we find a good agreement for anthracene with deviations of 9% and 4% for a - and b -direction, respectively. The results for pentacene differ more, showing an overestimation of the mobility by roughly 26% by the NN driven simulations. However, both the reference and the ML values are too large relative to experimentally determined results. Employing NN models trained on gradients from higher level DFTB or DFT, that would lead to higher reorganization energies, shows the expected trend of decreasing the mobilities. Δ -LC and Δ -B3LYP lead to almost the same reorganization energies, which is also reflected in the mobility values. For the small (ANT-a) and medium (ANT-b) mobility cases, results with Δ - ω B97X gradients are improved but the mobility is still overestimated by a factor of approximately 2. In the high mobility case of pentacene the mobility is already much closer to the experiment using Δ -LC forces, which lead to an overestimation of 30%.

3.2.2 Comparison of Computational Costs

Here we assess the performance of the learned models in respect of simulation time. To compare timings with the different methods and models we ran 100 trajectories with only two molecules for 1000 steps of NAMD simulation with the exact same settings compared to our previous calculations. The timings are estimated as averages of time spent on single calculations of site energies plus respective gradients and for couplings. For gradients in the Δ approach timings were averaged on the training-data calculations. All computations are performed on single CPU cores of Intel Xeon Silver 4214 @ 2.200 GHz processors.

Table 4: Comparison of timings (in ms) for the calculation of diagonal Hamiltonian elements (site energies) plus gradients in anthracene and pentacene with DFTB, DFT and NN models.

Molecule	Type	DFTB		DFT		NN
		FMO	Δ -LC	Δ -B3LYP	Δ - ω B97X	
ANT	diag	3.200	7.935×10^2	2.148×10^6	3.681×10^6	0.500
PEN	diag	1.020×10^1	2.753×10^3	- -	- -	0.900

Table 5: Comparison of timings (in ms) for the calculation of off-diagonal Hamiltonian elements (couplings) in anthracene and pentacene with DFTB and NN-models.

Molecule	FMO-DFTB	NN
ANT	1.700	0.100
PEN	3.800	0.200

The computational cost of diagonal Hamiltonian elements plus gradients in the FMO scheme is reduced by about one order of magnitude when turning from DFTB to neural network models. The same is true for off-diagonal Hamiltonian elements in the FMO approach. For the much more costly gradients calculated with LC-DFTB2, the respective neural network models outperform DFTB by more than three orders of magnitude. Additionally, the favorable N^2 scaling with the system size (N being the number of atoms) of the NN models

compared to the N^3 scaling of DFTB becomes apparent when comparing timings for anthracene (24 atoms) to pentacene (36 atoms). Switching to DFT gradients, the speedup for the NN models is about seven orders of magnitude.

4 Conclusion

Acknowledgement

M.K., P.M.D. and M.E. gratefully acknowledge financial support by the German Research Foundation (DFG) through the Research Training Group 2450 “Tailored Scale-Bridging Approaches to Computational Nanoscience”. W.X. acknowledges support through the “Virtual Materials Design” (VIRTMAT) project. Additional support by the state of Baden-Württemberg through bwHPC and the German Research Foundation (DFG) through grant no INST 40/575-1 FUGG (JUSTUS 2 cluster) is appreciated.

Supporting Information Available

References

- (1) Armstrong, N. R.; Wang, W.; Alloway, D. M.; Placencia, D.; Ratcliff, E.; Brumbach, M. Organic/Organic Heterojunctions: Organic Light Emitting Diodes and Organic Photovoltaic Devices. *Macromol. Rapid Commun.* **2009**, *30*, 717–731.
- (2) Meerheim, R.; Lussem, B.; Leo, K. Efficiency and Stability of Pin Type Organic Light Emitting Diodes for Display and Lighting Applications. *Proc. IEEE* **2009**, *97*, 1606–1626.
- (3) Kulkarni, A. P.; Tonzola, C. J.; Babel, A.; Jenekhe, S. A. Electron Transport Materials for Organic Light-Emitting Diodes. *Chem. Mater.* **2004**, *16*, 4556–4573.

- (4) Dimitrakopoulos, C. D.; Malenfant, P. R. Organic Thin Film Transistors for Large Area Electronics. *Adv. Mater.* **2002**, *14*, 99–117.
- (5) Newman, C. R.; Frisbie, C. D.; da Silva Filho, D. A.; Brédas, J.-L.; Ewbank, P. C.; Mann, K. R. Introduction to Organic Thin Film Transistors and Design of N-Channel Organic Semiconductors. *Chem. Mater.* **2004**, *16*, 4436–4451.
- (6) Facchetti, A. Semiconductors for Organic Transistors. *Mater. Today* **2007**, *10*, 28–37.
- (7) Kippelen, B.; Brédas, J.-L. Organic Photovoltaics. *Energy Env. Sci* **2009**, *2*, 251–261.
- (8) Dennler, G.; Scharber, M. C.; Brabec, C. J. Polymer-Fullerene Bulk-Heterojunction Solar Cells. *Adv. Mater.* **2009**, *21*, 1323–1338.
- (9) Deibel, C.; Dyakonov, V. Polymer–Fullerene Bulk Heterojunction Solar Cells. *Rep. Prog. Phys.* **2010**, *73*, 096401.
- (10) Dey, A.; Singh, A.; Das, D.; Iyer, P. K. In *Thin Film Structures in Energy Applications*; Babu Krishna Moorthy, S., Ed.; Springer International Publishing: Cham, 2015; pp 97–128.
- (11) Oberhofer, H.; Reuter, K.; Blumberger, J. Charge Transport in Molecular Materials: An Assessment of Computational Methods. *Chem. Rev.* **2017**, *117*, 10319–10357.
- (12) Kubař, T.; Gutiérrez, R.; Kleinekathöfer, U.; Cuniberti, G.; Elstner, M. Modeling Charge Transport in DNA Using Multi-Scale Methods. *Phys. Status Solidi B* **2013**, *250*, 2277–2287.
- (13) Heck, A.; Kranz, J. J.; Kubař, T.; Elstner, M. Multi-Scale Approach to Non-Adiabatic Charge Transport in High-Mobility Organic Semiconductors. *J. Chem. Theory Comput.* **2015**, *11*, 5068–5082.
- (14) Kranz, J. J.; Elstner, M. Simulation of Singlet Exciton Diffusion in Bulk Organic Materials. *J. Chem. Theory Comput.* **2016**, *12*, 4209–4221.

- (15) Giannini, S.; Carof, A.; Ellis, M.; Yang, H.; Ziogos, O. G.; Ghosh, S.; Blumberger, J. Quantum Localization and Delocalization of Charge Carriers in Organic Semiconducting Crystals. *Nat. Commun.* **2019**, *10*, 1–12.
- (16) Lederer, J.; Kaiser, W.; Mattoni, A.; Gagliardi, A. Machine Learning–Based Charge Transport Computation for Pentacene. *Adv. Theory Simul.* **2019**, *2*, 1800136–1800136.
- (17) Wang, C.-I.; Braza, M. K. E.; Claudio, G. C.; Nellas, R. B.; Hsu, C.-P. Machine Learning for Predicting Electron Transfer Coupling. *J. Phys. Chem. A* **2019**, *123*, 7792–7802.
- (18) Krämer, M.; Dohmen, P. M.; Xie, W.; Holub, D.; Christensen, A. S.; Elstner, M. Charge and Exciton Transfer Simulations Using Machine-Learned Hamiltonians. *J. Chem. Theory Comput.* **2020**, *16*, 4061–4070.
- (19) Musil, F.; De, S.; Yang, J.; Campbell, J. E.; Day, G. M.; Ceriotti, M. Machine Learning for the Structure–Energy–Property Landscapes of Molecular Crystals. *Chem. Sci.* **2018**, *9*, 1289–1300.
- (20) Çaylak, O.; Yaman, A.; Baumeier, B. Evolutionary Approach to Constructing a Deep Feedforward Neural Network for Prediction of Electronic Coupling Elements in Molecular Materials. *J. Chem. Theory Comput.* **2019**, *15*, 1777–1784.
- (21) Häse, F.; Valleau, S.; Pyzer-Knapp, E.; Aspuru-Guzik, A. Machine Learning Exciton Dynamics. *Chem. Sci.* **2016**, *7*, 5139–5147.
- (22) Li, J.; Reiser, P.; Boswell, B. R.; Eberhard, A.; Burns, N. Z.; Friederich, P.; Lopez, S. A. Automatic Discovery of Photoisomerization Mechanisms with Nanosecond Machine Learning Photodynamics Simulations. *Chem. Sci.* **2021**,
- (23) Westermayr, J.; Gastegger, M.; Menger, M. F. S. J.; Mai, S.; González, L.; Marque-

- tand, P. Machine Learning Enables Long Time Scale Molecular Photodynamics Simulations. *Chem. Sci.* **2019**, *10*, 8100–8107.
- (24) Westermayr, J.; Marquetand, P. Machine Learning and Excited-State Molecular Dynamics. *Mach. Learn.: Sci. Technol.* **2020**, *1*, 043001.
- (25) Westermayr, J.; Gastegger, M.; Marquetand, P. Combining SchNet and SHARC: The SchNarc Machine Learning Approach for Excited-State Dynamics. *J. Phys. Chem. Lett.* **2020**, *11*, 3828–3834.
- (26) Porezag, D.; Frauenheim, T.; Köhler, T.; Seifert, G.; Kaschner, R. Construction of Tight-Binding-like Potentials on the Basis of Density-Functional Theory: Application to Carbon. *Phys. Rev. B* **1995**, *51*, 12947.
- (27) Seifert, G.; Porezag, D.; Frauenheim, T. Calculations of Molecules, Clusters, and Solids with a Simplified LCAO-DFT-LDA Scheme. *Int. J. Quantum Chem.* **1996**, *58*, 185–192.
- (28) Elstner, M.; Porezag, D.; Jungnickel, G.; Elsner, J.; Haugk, M.; Frauenheim, T.; Suhai, S.; Seifert, G. Self-Consistent-Charge Density-Functional Tight-Binding Method for Simulations of Complex Materials Properties. *Phys. Rev. B* **1998**, *58*, 7260.
- (29) Niehaus, T. A.; Suhai, S.; Della Sala, F.; Lugli, P.; Elstner, M.; Seifert, G.; Frauenheim, T. Tight-Binding Approach to Time-Dependent Density-Functional Response Theory. *Phys. Rev. B* **2001**, *63*, 085108.
- (30) Kranz, J. J.; Elstner, M.; Aradi, B.; Frauenheim, T.; Lutsker, V.; Garcia, A. D.; Niehaus, T. A. Time-Dependent Extension of the Long-Range Corrected Density Functional Based Tight-Binding Method. *J. Chem. Theory Comput.* **2017**, *13*, 1737–1747.
- (31) Aradi, B.; Hourahine, B.; Frauenheim, T. DFTB+, a Sparse Matrix-Based Implementation of the DFTB Method. *J. Phys. Chem A* **2007**, *111*, 5678–5684.

- (32) Hourahine, B.; Aradi, B.; Blum, V.; Bonafé, F.; Buccheri, A.; Camacho, C.; Cevallos, C.; Deshayes, M. Y.; Dumitrică, T.; Dominguez, A.; Ehlert, S.; Elstner, M.; van der Heide, T.; Hermann, J.; Irle, S.; Kranz, J. J.; Köhler, C.; Kowalczyk, T.; Kubař, T.; Lee, I. S.; Lutsker, V.; Maurer, R. J.; Min, S. K.; Mitchell, I.; Negre, C.; Niehaus, T. A.; Niklasson, A. M. N.; Page, A. J.; Pecchia, A.; Penazzi, G.; Persson, M. P.; Řezáč, J.; Sánchez, C. G.; Sternberg, M.; Stöhr, M.; Stuckenberg, F.; Tkatchenko, A.; Yu, V. W.-z.; Frauenheim, T. DFTB+, a Software Package for Efficient Approximate Density Functional Theory Based Atomistic Simulations. *J. Chem. Phys.* **2020**, *152*, 124101.
- (33) Christensen, A. S.; Faber, F. A.; von Lilienfeld, O. A. Operators in Quantum Machine Learning: Response Properties in Chemical Space. *J. Chem. Phys.* **2019**, *150*, 064105.
- (34) Kubař, T.; Elstner, M. A Hybrid Approach to Simulation of Electron Transfer in Complex Molecular Systems. *J R Soc Interface* **2013**, *10*, 20130415.
- (35) Kitaura, K.; Ikeo, E.; Asada, T.; Nakano, T.; Uebayasi, M. Fragment Molecular Orbital Method: An Approximate Computational Method for Large Molecules. *Chem. Phys. Lett.* **1999**, *313*, 701–706.
- (36) Kubař, T.; Woiczikowski, P. B.; Cuniberti, G.; Elstner, M. Efficient Calculation of Charge-Transfer Matrix Elements for Hole Transfer in DNA. *J. Phys. Chem. B* **2008**, *112*, 7937–7947.
- (37) Ehrenfest, P. Bemerkung Über Die Angenäherte Gültigkeit Der Klassischen Mechanik Innerhalb Der Quantenmechanik. *Z. Phys.* **1927**, *45*, 455–457.
- (38) McLachlan, A. A Variational Solution of the Time-Dependent Schrodinger Equation. *Mol. Phys.* **1964**, *8*, 39–44.
- (39) Tully, J. C. Molecular Dynamics with Electronic Transitions. *J. Chem. Phys.* **1990**, *93*, 1061–1071.

- (40) Carof, A.; Giannini, S.; Blumberger, J. Detailed Balance, Internal Consistency, and Energy Conservation in Fragment Orbital-Based Surface Hopping. *J. Chem. Phys.* **2017**, *147*, 214113.
- (41) Akimov, A. V.; Prezhdo, O. V. The PYXAID Program for Non-Adiabatic Molecular Dynamics in Condensed Matter Systems. *J. Chem. Theory Comput.* **2013**, *9*, 4959–4972.
- (42) Mason, R. The Crystallography of Anthracene at 95°C and 290°C. *Acta Crystallogr.* **1964**, *17*, 547–555.
- (43) Wang, J.; Wolf, R. M.; Caldwell, J. W.; Kollman, P. A.; Case, D. A. Development and Testing of a General Amber Force Field. *J. Comput. Chem.* **2004**, *25*, 1157–1174.
- (44) Wang, J.; Wang, W.; Kollman, P. A.; Case, D. A. Automatic Atom Type and Bond Type Perception in Molecular Mechanical Calculations. *J. Mol. Graph. Model.* **2006**, *25*, 247–260.
- (45) Singh, U. C.; Kollman, P. A. An Approach to Computing Electrostatic Charges for Molecules. *J. Comput. Chem.* **1984**, *5*, 129–145.
- (46) Besler, B. H.; Merz, K. M.; Kollman, P. A. Atomic Charges Derived from Semiempirical Methods. *J. Comput. Chem.* **1990**, *11*, 431–439.
- (47) Petersson, G. A.; Bennett, A.; Tensfeldt, T. G.; Al-Laham, M. A.; Shirley, W. A.; Mantzaris, J. A Complete Basis Set Model Chemistry. I. The Total Energies of Closed-Shell Atoms and Hydrides of the First-Row Elements. *J. Chem. Phys.* **1988**, *89*, 2193–2218.
- (48) Petersson, G. A.; Al-Laham, M. A. A Complete Basis Set Model Chemistry. II. Open-Shell Systems and the Total Energies of the First-Row Atoms. *J. Chem. Phys.* **1991**, *94*, 6081–6090.

- (49) Frisch, M. J.; Trucks, G. W.; Schlegel, H. B.; Scuseria, G. E.; Robb, M. A.; Cheeseman, J. R.; Scalmani, G.; Barone, V.; Mennucci, B.; Petersson, G. A.; Nakatsuji, H.; Caricato, M.; Li, X.; Hratchian, H. P.; Izmaylov, A. F.; Bloino, J.; Zheng, G.; Sonnenberg, J. L.; Hada, M.; Ehara, M.; Toyota, K.; Fukuda, R.; Hasegawa, J.; Ishida, M.; Nakajima, T.; Honda, Y.; Kitao, O.; Nakai, H.; Vreven, T.; Montgomery Jr., J. A.; Peralta, J. E.; Ogliaro, F.; Bearpark, M. J.; Heyd, J.; Brothers, E. N.; Kudin, K. N.; Staroverov, V. N.; Kobayashi, R.; Normand, J.; Raghavachari, K.; Rendell, A. P.; Burant, J. C.; Iyengar, S. S.; Tomasi, J.; Cossi, M.; Rega, N.; Millam, N. J.; Klene, M.; Knox, J. E.; Cross, J. B.; Bakken, V.; Adamo, C.; Jaramillo, J.; Gomperts, R.; Stratmann, R. E.; Yazyev, O.; Austin, A. J.; Cammi, R.; Pomelli, C.; Ochterski, J. W.; Martin, R. L.; Morokuma, K.; Zakrzewski, V. G.; Voth, G. A.; Salvador, P.; Dannenberg, J. J.; Dapprich, S.; Daniels, A. D.; Farkas, Ö.; Foresman, J. B.; Ortiz, J. V.; Cioslowski, J.; Fox, D. J. *Gaussian 09*; Gaussian, Inc.: Wallingford, CT, USA, 2009.
- (50) Evans, D. J.; Holian, B. L. The Nose–Hoover Thermostat. *J. Chem. Phys.* **1985**, *83*, 4069.
- (51) Berendsen, H. J. C.; van der Spoel, D.; van Drunen, R. GROMACS: A Message-Passing Parallel Molecular Dynamics Implementation. *Comput. Phys. Commun.* **1995**, *91*, 43–56.
- (52) Abraham, M. J.; Murtola, T.; Schulz, R.; Páll, S.; Smith, J. C.; Hess, B.; Lindahl, E. GROMACS: High Performance Molecular Simulations through Multi-Level Parallelism from Laptops to Supercomputers. *SoftwareX* **2015**, *1–2*, 19–25.
- (53) Niehaus, T. A.; Della Sala, F. Range Separated Functionals in the Density Functional Based Tight-Binding Method: Formalism. *Phys. Status Solidi B* **2012**, *249*, 237–244.
- (54) Becke, A. D. Becke’s three parameter hybrid method using the LYP correlation functional. *J. Chem. Phys.* **1993**, *98*, 5648–5652.

- (55) Chai, J.-D.; Head-Gordon, M. Systematic optimization of long-range corrected hybrid density functionals. *J. Chem. Phys.* **2008**, *128*, 084106.
- (56) Weigend, F.; Ahlrichs, R. Balanced basis sets of split valence, triple zeta valence and quadruple zeta valence quality for H to Rn: Design and assessment of accuracy. *Phys. Chem. Chem. Phys.* **2005**, *7*, 3297–3305.
- (57) Weigend, F. Accurate Coulomb-fitting basis sets for H to Rn. *Phys. Chem. Chem. Phys.* **2006**, *8*, 1057–1065.
- (58) Neese, F. The ORCA program system. *Wiley Interdiscip. Rev. Comput. Mol. Sci.* **2012**, *2*, 73–78.
- (59) Neese, F. Software update: the ORCA program system, version 4.0. *Wiley Interdiscip. Rev. Comput. Mol. Sci.* **2018**, *8*, e1327.
- (60) Zhao, H.; Liu, F.; Li, L.; Luo, C. A Novel Softplus Linear Unit for Deep Convolutional Neural Networks. *Appl Intell* **2018**, *48*, 1707–1720.
- (61) Martín Abadi,; Ashish Agarwal,; Paul Barham,; Eugene Brevdo,; Zhifeng Chen,; Craig Citro,; Greg S. Corrado,; Andy Davis,; Jeffrey Dean,; Matthieu Devin,; Sanjay Ghemawat,; Ian Goodfellow,; Andrew Harp,; Geoffrey Irving,; Michael Isard,; Jia, Y.; Rafal Jozefowicz,; Lukasz Kaiser,; Manjunath Kudlur,; Josh Levenberg,; Dan Mané,; Rajat Monga,; Sherry Moore,; Derek Murray,; Chris Olah,; Mike Schuster,; Jonathon Shlens,; Benoit Steiner,; Ilya Sutskever,; Kunal Talwar,; Paul Tucker,; Vincent Vanhoucke,; Vijay Vasudevan,; Fernanda Viégas,; Oriol Vinyals,; Pete Warden,; Martin Wattenberg,; Martin Wicke,; Yuan Yu,; Xiaoqiang Zheng, *TensorFlow: Large-Scale Machine Learning on Heterogeneous Systems*; 2015.
- (62) Chollet, F., et al. Keras. 2015.

- (63) Kingma, D. P.; Ba, J. Adam: A Method for Stochastic Optimization. *ArXiv14126980 Cs* **2017**,
- (64) Li, L.; Jamieson, K.; DeSalvo, G.; Rostamizadeh, A.; Talwalkar, A. Hyperband: A Novel Bandit-Based Approach to Hyperparameter Optimization. *ArXiv160306560 Cs Stat* **2018**,
- (65) Kubo, R.; Toda, M.; Hashitsume, N. *Statistical physics II: nonequilibrium statistical mechanics*; Springer Science & Business Media, 2012; Vol. 31.
- (66) Frenkel, D.; Smit, B. *Understanding molecular simulation: From algorithms to applications*; Computational Sciences Series; Elsevier (formerly published by Academic Press), 2002; Vol. 1; pp 1–638.
- (67) Grandbois, M.; Beyer, M.; Rief, M.; Clausen-Schaumann, H.; Gaub, H. E. How Strong Is a Covalent Bond? *Science* **1999**, *283*, 1727–1730.
- (68) Karl, N.; Marktanner, J. Electron and hole mobilities in high purity anthracene single crystals. *Mol. Cryst. Liq. Cryst. A* **2001**, *355*, 149–173.
- (69) Jurchescu, O. D.; Baas, J.; Palstra, T. T. Effect of impurities on the mobility of single crystal pentacene. *Appl. Phys. Lett.* **2004**, *84*, 3061–3063.

For Table of Contents Only

